



Microwave irradiation induced UIO-66-NH₂ anchored on graphene with high activity for photocatalytic reduction of CO₂

Xiaojun Wang^a, Xiaolong Zhao^b, Dieqing Zhang^b, Guisheng Li^{b,*,}, Hexing Li^{a,b,*}

^a College of Environmental and Chemical Engineering, Shanghai University of Electric Power, Shanghai 201300, China

^b Key Laboratory of Resource Chemistry of Ministry of Education, Shanghai Key Laboratory of Rare Earth Functional Materials, Shanghai Normal University, Shanghai 200234, China



ARTICLE INFO

Keywords:
Microwave
UIO-66-NH₂
Graphene
Photocatalytic
CO₂
Photo-reduction

ABSTRACT

Carbon dioxide (CO₂), as a kind of the greenhouse gas, was highly desirable to be converted into fuels by using solar energy. Herein, a novel microwave-induced synthesis route was explored for the in-situ growth and assemble of highly dispersed UIO-66-NH₂ nanocrystals onto graphene (GR) with the formation of highly active photocatalyst for converting CO₂. The as-obtained UIO-66-NH₂/GR hybrid exhibited both high activity and selectivity in the photocatalytic reduction of CO₂ to formic acid under visible-light irradiation ($\lambda > 410$ nm, 300 W Xe lamp). The photo-reduction efficiency of CO₂ for UIO-66-NH₂/GR was about 11 times of that for the pure UIO-66-NH₂, and 2 times of as that for the UIO-66-NH₂/GR sample obtained via traditional hydrothermal synthesis. The proposed microwave-assisted synthesis route may produce lots of "super hot spots" (SHS) on the surface of GR. These SHS not only resulted in small UIO-66-NH₂ nanocrystals with a high dispersion onto the surface of GR, but also can greatly improve the interaction between UIO-66-NH₂ and GR. Such highly dispersed UIO-66-NH₂ ultrafine nanocrystals can allow more active surface for both trapping CO₂ and enhancing the light absorption capability to generate photogenerated electrons from UIO-66-NH₂ frameworks for reducing CO₂ molecules. The strong UIO-66-NH₂/GR interaction can effectively facilitate the photoelectron-hole separation and inhibit the leaching of UIO-66-NH₂ from GR, contributing a high CO₂ photo-reduction activity and excellent recyclability. Such work supplied a novel route for constructing strong interaction between MOFs and graphene with the aim at efficiently reducing CO₂ under visible-light irradiation. It could also be explored for other applications, including N₂ reduction, water-splitting, and solar cells.

1. Introduction

The emission of carbon dioxide into the atmosphere from the combustion of fossil fuels caused a series of environment and energy issues [1–3]. Reduction of carbon dioxide to useful chemicals was considered as a feasible solution to the depletion of fossil fuels as well as a way of alleviation of CO₂ emissions [4,5]. Using solar energy to convert CO₂ into hydrocarbon fuels by water was a sustainable process for human beings [6]. The photocatalytic CO₂ reduction by using water as proton source obtained great attention owing to its direct using sunlight as the energy source [7]. Large number of studies focusing on CO₂ photo-reduction, including heterogeneous semiconductor systems and homogeneous transition metal-based complexes which had been investigated but challenges still remained [8–12]. TiO₂-based photocatalysts had been intensively investigated owing to their stability and

availability at low cost [13–15]. Unfortunately, their efficiency of CO₂ photo-reduction was not satisfactory because of the weak CO₂ adsorption on the catalyst surface and the requirement of UV light for driving the photocatalytic reaction [16,17].

To enhance the capability of CO₂ capture and its photocatalytic conversion using solar energy, metal-organic frameworks (MOFs) could be an ideal candidate for photo-reduction of CO₂ [18–22]. UIO-66-NH₂ as a common MOFs was widely studied owing to its high thermal stability [23,24], large surface area and strong CO₂ absorption capacity [25–27]. Thus, it would be an excellent platform for CO₂ photoreduction [28–30]. However, it still suffered some limitations from its poor conductivity and weak visible light response [31,32]. Forming composites via binding MOFs with other functional materials supplied a route for overcoming such limitations [33]. It was known that graphene has unique two-dimensional structure and outstanding electrical,

* Corresponding author at: Key Laboratory of Resource Chemistry of Ministry of Education, Shanghai Key Laboratory of Rare Earth Functional Materials, Shanghai Normal University, Shanghai 200234, China.

** Corresponding author.

E-mail addresses: liguisheng@shnu.edu.cn (G. Li), hexing-li@shnu.edu.cn (H. Li).

optical and thermal properties with wide application in photovoltaic, electronics, capacitors and catalysis [34–37]. Liang et al. used graphene with less defective to enhance titania for photocatalytic reduction of CO_2 owing to the superior electrical mobility [38]. M/DOBDC (M = Mg^{2+} , Ni^{2+} , or Co^{2+} , DOBDC = 2,5-dioxido-1,4-benzene dicarboxylate) MOFs were also covalently linked to graphene with the formation of remarkable improvement in the mechanical properties and CO_2 uptake [39]. Therefore, constructing a hybrid through loading MOFs on graphene would be also favorable for enhancing the catalytic performance of MOFs [40,41]. However, how to make sure the fast electron transfer from MOFs to graphene was still challenging the researchers owing to the weak interactions between MOFs and graphene. Thus, it was highly required to explore effective route to fabricate graphene loaded MOFs.

Luckily, the microwave-irradiation induced solvothermal (MIS) treatment supplied an effective way for both fast fabricating MOFs structures [42] and uniformly coating TiO_2 layers on copper nanowires [43] or carbon nanotubes (CNT) [44] with strong interactions ($\text{Cu}/\text{CNT}-\text{TiO}_2$) through microwave-induced local "super hot" dots in our previous reports. Herein, the MIS route was further developed for the construction of $\text{UIO}-66-\text{NH}_2$ /graphene composites as a highly efficient photocatalyst for CO_2 photo-reduction. $\text{UIO}-66-\text{NH}_2$ was fast crystallized to MOFs crystals in 40 min, owing to the local "super hot" dots dispersed on the surface of graphene in the MIS process. The as-formed MOFs crystals possessed a small average size of 14.5 nm, with a high dispersion and strong junctions on the surface of graphene. The $\text{UIO}-66-\text{NH}_2/\text{GR}$ exhibited the maximum CO_2 uptake of about $73 \text{ cm}^3 \text{ g}^{-1}$. These properties provided an excellent performance for CO_2 photo-reduction to formic acid with a high selectivity (78.6%). Furthermore, the formic acid evolution rate of $\text{UIO}-66-\text{NH}_2/\text{GR}$ obtained via MIS process was about 11 times of that of the pure $\text{UIO}-66-\text{NH}_2$. Compared to the sample with the same composition obtained via traditional hydrothermal method, the MIS induced sample exhibited a greatly enhanced activity (108%) for the photo-reduction of CO_2 .

2. Experimental section

2.1. Preparation of photocatalysts

In a typical process for fabricating $\text{UIO}-66-\text{NH}_2/\text{GR}$ composite photocatalyst, GR (0.5–3.0 wt%) were highly dispersed in a 50 mL N,N -dimethylformamide (DMF) under ultrasonic irradiation. To the above solution, 90 mg 2-amino-terephthalic acid and 120 mg zirconium (IV) chloride were introduced with ultrasonication for another 30 min until 2-amino-terephthalic acid and zirconium (IV) chloride were completed dissolved [45]. The as-formed yellow-green transparent solution was immediately transferred into a 50 mL quartz vessel with a Teflon lid. The quartz vessel was heated under microwave irradiation in a microwave digestion system (Ethos TC, Milestone) at 120 °C for 40 min with a heating rate of 10 °C/min. The system was cooled down to room temperature within 30 min. Finally, dark-green powder was separated via centrifugation, washed with DMF, methanol, and ethanol each for 3 times. As-obtained samples were dried at 60 °C for 12 h in a vacuum drying oven. The as-obtained composite photocatalyst was named as $\text{UIO}-66-\text{NH}_2/\text{xGR}$, where x represents the mass percentage ratio of GR/ $\text{UIO}-66-\text{NH}_2$ (x = 0.5–3.0). For better comparison, pure $\text{UIO}-66-\text{NH}_2$ was also synthesized in the absence of GR under microwave irradiation while keeping other conditions unchanged. The sample of $\text{UIO}-66-\text{NH}_2/2.0\text{GR}$ was also prepared via the traditional hydrothermal method at 120 °C for 24 h in a Teflon autoclave while keeping other conditions unchanged. Meanwhile, $\text{UIO}-66-\text{NH}_2/2.0\text{GR}$ composites were also prepared through mechanically mixing the pure $\text{UIO}-66-\text{NH}_2$ and GR with the same GR weight percentage.

2.2. Characterization

The crystal phase of the samples was analyzed by using X-ray diffraction patterns (2 theta varied from 3° to 50°), using a Rigaku Dmax-3C Advance X-ray diffractometer ($\text{CuK}\alpha$ radiation, $\lambda = 1.5406 \text{ \AA}$). The N_2 adsorption-desorption isotherms were measured at 77 K using a Micromeritics ASAP 2010 instrument, from which, the specific surface area (S_{BET}) and pore volume (VP) were calculated by applying Brunauer-Emmett-Teller (BET) and Barrett-Joyner-Halenda (BJH) models [46], respectively. Field emission scanning electron microscopy (FESEM, JEOL JSM-6700) and transmission electron microscopy (JEM-2010) were employed to observe particle size and morphology. Raman spectra and UV-vis diffuse reflectance spectra (UV-vis DRS) were collected on Dilor Super LabRam II and MC-2530 instruments, respectively. The CO_2 adsorption isotherms desorption was analyzed by BELSORP-max at atmospheric pressure with the temperature of 273 K.

2.3. Photoelectrochemical (PEC) measurements

Photoelectrochemical measurements were performed in a conventional three-electrode set up in a homemade single-compartment quartz cell on an electrochemical station (CHI 660E). A 300 W Xe lamp with an ultraviolet filter ($\lambda > 410 \text{ nm}$) was used as the visible-light source and was positioned 10 cm away from the photoelectrochemical cell. The sample of photocatalyst was coated on the FTO served as work electrode with an active area of 4 cm^2 . The 100 mg of photocatalyst was mixed with 20 mg of polyethylene glycol (PEG, MW 20000) and 200 μL of ethanol, followed by coating the photocatalysis on the conductive surface of the FTO with a doctor blade method. Then the coated FTO conductive glasses were dried at room temperature and calcined at 200 °C for 2 h in N_2 atmosphere. In the PEC measurements, platinum sheets (99.99%, 20.0 mm × 20.0 mm × 0.2 mm) were served as a counter electrode. Saturated calomel electrode (SCE) was used as a reference electrode. Na_2SO_4 (0.5 mol/L) was used as the electrolyte for the photoelectrochemical measurements [47]. The photocurrent was detected by using the visible-light ($\lambda > 410 \text{ nm}$, 300 W Xe lamp) on-off process with a pulse of 20 s on-off cycle at a bias voltage of 0.5 V (vs. SCE) by chronoamperometry [48]. Electrochemical impedance spectroscopy (EIS) measurements were collected under visible-light illumination ($\lambda > 410 \text{ nm}$, 300 W Xe lamp) by using an ultraviolet filter in a 0.5 mol/L Na_2SO_4 solution at open circuit voltage over a frequency range from 10^5 to 10^{-1} Hz with an AC voltage at 5 mV. The Mott-Schottky plots were obtained at a fixed frequency of 1 kHz to determine the flat-band potential and carrier density.

2.4. Photocatalytic activity for the reduction of CO_2

Photocatalytic CO_2 reductions tests were carried out at 25 °C in a homemade glass reactor, containing 20.0 mg catalyst, 40 mL DMF as the solvent of CO_2 , 5 mL triethanolamine (TEOA) as the sacrificial agent, and 3 mL H_2O as the proton source for CO_2 photo-reduction under visible-light irradiation ($\lambda > 410 \text{ nm}$, 300 W Xe lamp) by using an ultraviolet filter for 4 h [49,50]. Before light illumination, the homemade glass reactor filled with the above aqueous solution mixture was bubbled with the mixture gas (50% Ar and 50% CO_2) for 30 min, then the photocatalytic reactor was irradiated by visible-light. The light source was located at 10 cm away from the solution surface (Scheme S1.). After 4 h of illumination, 0.5 mL of sampled gas was analyzed by using a gas chromatograph (GC9800 Shanghai Ke Chuang Chromatograph Instruments Co. Ltd., China, TCD, with Argon (99.999%) as the carrier gas with TDX-1 columns) to detected hydrogen. The liquid product of formic acid was detected by ion chromatography (ICS-5000, IonPacAS11-HC, 4 × 250 mm) and the reduction amount of CO_2 was detected by gas chromatograph (GC9800, Shanghai Ke Chuang Chromatograph Instruments Co. Ltd., China, TCD, with Helium (99.999%) as the carrier gas with 5A molecular sieve columns). Other gas product

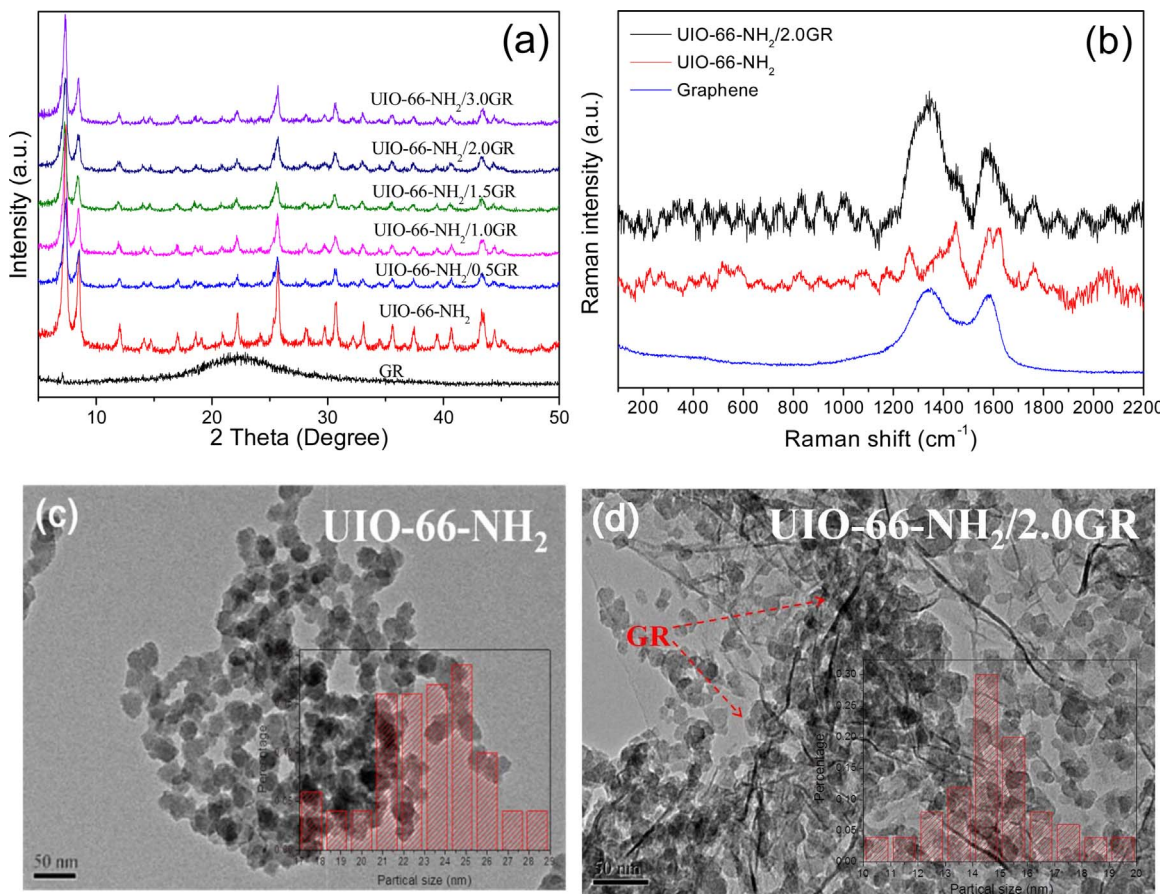


Fig. 1. (a) The XRD patterns of GR and UIO-66-NH₂/GR composites, (b) the Raman spectra of the GR before and after loading UIO-66-NH₂ via MIS route, recorded under excitation at $\lambda_{\text{exc}} = 633$ nm and the TEM images of (c) UIO-66-NH₂ and (d) UIO-66-NH₂/2.0GR synthesized by MIS route.

of the CO₂ photo-reduction was detected by gas chromatograph with FID detector (GC2002, Shanghai Ke Chuang Chromatograph Instruments Co. Ltd., China, FID, with Nitrogen (99.999%) as the carrier gas with 25% squalane columns) to detect CH₄.

3. Results and discussion

As shown in Fig. 1a, the crystallinity of the as-obtained UIO-66-NH₂/GR was evaluated by power X-ray diffraction (XRD). The feature peaks of these synthesized composite at $\sim 5^\circ$ and $\sim 8^\circ$ agreed quite well with the XRD pattern of UIO-66-NH₂ framework [51]. The high intensity of the XRD characteristic peaks indicated a highly crystalline structure for UIO-66-NH₂ synthesized by the process of MIS. However, nearly no obvious characteristic peaks of GR were observed in the UIO-66-NH₂/GR samples. This could be attributed to the low content and high dispersion of GR. For better illustrating the existence of GR in the as-obtained sample, Raman spectra was recorded *via* visible light excitation ($\lambda = 633$ nm). As shown in Fig. 1b, pure GR exhibited a typical in-phase vibration of the graphite lattice (G band) at 1575 cm^{-1} and a disorder band owing to the graphite edges (D band) at approximately 1355 cm^{-1} [52,53]. Upon loading UIO-66-NH₂ crystals, it was universally observed that both the G and the D bands were broadened. The G and D bands of UIO-66-NH₂/3.0GR was also illustrated in Fig. S3. These results suggested a strong interaction formed between UIO-66-NH₂ and the surface of GR during the microwave-assisted synthesis process. For better investigating the micro-nano scaled morphology, TEM was also utilized to analyze the as-formed samples. As shown in Fig. S1, pure GR exhibited a two-dimensional structure with micro-meter-long wrinkles. The TEM image of the pure UIO-66-NH₂ (Fig. 1c) indicated that the pure UIO-66-NH₂ nanoparticle synthesis by

microwave-assisted suffered a serious aggregation. As shown in the inset graph of Fig. 1c, the average size of the UIO-66-NH₂ nanoparticle was about 23.5 nm. Fortunately, such aggregation could be well avoided by introducing GR as a supporter for trapping UIO-66-NH₂ under microwave-assisted synthesis process. As shown in Fig. 1d, the sample of UIO-66-NH₂/2.0GR exhibited a uniform dispersed of UIO-66-NH₂ nanocrystals on the surface of GR. Furthermore, introducing GR also decreased the particle size of UIO-66-NH₂ from 23.5 nm to 14.5 nm in average. Other UIO-66-NH₂/GR composites also possessed a well dispersion on the surface of GR (Fig. S2). These results suggested that GR may work as an excellent microwave adsorbent owing to its high strong absorption coefficient. Thus, it was favorable for the fabrication of UIO-66-NH₂ MOFs nanocrystals with high dispersity and small average size on the surface of GR [54]. As shown in Fig. S4, the HRTEM image exhibited an octahedral structure of UIO-66-NH₂ on the surface of GR. It was also noted that porous structures existed in the bulk of the UIO-66-NH₂ MOFs crystals.

The surface area and porosity of these as-obtained samples were analyzed by N₂ adsorption-desorption measurements carried out at 77 K. As shown in Fig. 2a, the sample of GR exhibited a typical pore structure of graphene oxide with a BET surface area of $700.0\text{ m}^2/\text{g}$ (Table S1). Meanwhile, it was noted that the as-obtained pure UIO-66-NH₂ exhibited a large surface area of $968.9\text{ m}^2/\text{g}$ and a typical Type IV isotherm suggested a mesoporous structure (average pore size = 2.1 nm) [55]. Upon introducing 2.0 wt% GR in to the synthesis system, a slight decrease of surface area from $968.9\text{ m}^2/\text{g}$ to $791.2\text{ m}^2/\text{g}$ was observed to the case of UIO-66-NH₂/2.0GR. Nevertheless, the isotherm for this sample still exhibited a higher adsorption amount of N₂ at relative pressures (P/P_0) approaching 1.0 compared to the pure UIO-66-NH₂. This implied the formation of large pores in the presence of

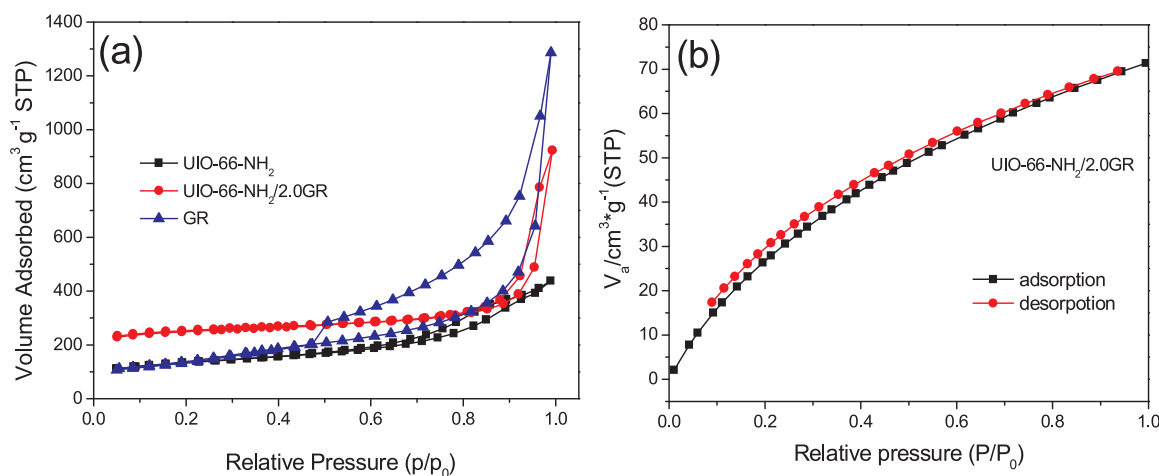


Fig. 2. (a) The nitrogen adsorption–desorption isotherms and pore distribution for the GR, UIO-66-NH₂, and UIO-66-NH₂/2.0GR and (b) CO₂ adsorption/desorption isotherms of UIO-66-NH₂/2.0GR.

reduced graphene with UIO-66-NH₂. Meanwhile, the large surface area (791.2 m²/g) was high enough for effectively trapping CO₂ molecules via physicochemical adsorption. From Table S1, it was clear that the surface area of the UIO-66-NH₂/GR sample was continuously decreased if the concentration of GR was over than 2.0 wt%. Furthermore, to understand the CO₂ adsorption ability of the sample a measurement of CO₂ adsorption isotherms desorption was analyzed by BELSORP-max. As shown in Fig. 2b, at atmospheric pressure and 273 K [56], the maximum CO₂ uptake for UIO-66-NH₂/2.0GR was 73 cm³ g⁻¹, which was beneficial for CO₂ photo-reduction. Owing to the presence of amino groups in the MOFs structure of UIO-66-NH₂, the sample of UIO-66-NH₂/2.0GR exhibited an excellent CO₂ adsorption ability. As known, these amino groups may serve as basic sites for absorbing more CO₂ molecule, thus the sample of UIO-66-NH₂/2.0GR exhibited an excellent CO₂ adsorption ability.

To understand the photocatalytic performance of UIO-66-NH₂/GR, these samples were characterized by UV-vis spectroscopy in diffuse reflectance (DR) mode. The DR-UV-vis spectra of UIO-66-NH₂ and UIO-66-NH₂/2.0GR were presented in Fig. 3a. The UIO-66-NH₂/2.0GR sample possessed an obvious enhanced absorption intensity in visible-light region compared to the sample of UIO-66-NH₂. It could be attributed to the introduction of GR to the UIO-66-NH₂, such was known that the introduce of GR could enhance the utilization efficiency of visible light [57]. According to the Kubelka-Munk function [58,59], the band gap of UIO-66-NH₂ and UIO-66-NH₂/2.0GR were calculated to be about 2.73 eV and 2.64 eV, respectively, via analyzing the relationship

between $(\alpha h\nu)^{1/2}$ and photon energy used as Tauc plots (Fig. 3b). To further study the photoelectrochemical properties of these samples, a series of photoelectrochemical measurements were tested. Fig. 4a showed the photocurrent responses of both UIO-66-NH₂ and UIO-66-NH₂/2.0GR were measured under visible-light ($\lambda > 410$ nm) irradiation at a constant potential of 0.5 V (vs. SCE). UIO-66-NH₂ displayed a low photocurrent intensity about 0.2 μ A/cm². Moreover, the photocurrent intensity was further improved to 0.5 μ A/cm² in the presence of GR. The enhancement of the photocurrent for UIO-66-NH₂/2.0GR could be attributed to the strong visible-light absorption capability and low photogenerated electron-hole pairs recombination rate. As known, higher photogenerated carrier density could be obtained in the presence of strong visible-light response and low photogenerated electron-hole pairs recombination rate. Electrochemical impedance spectroscopy (EIS) measurements were further performed for investigating the charge transfer process between graphene and UIO-66-NH₂. The capacitance arc of the EIS Nyquist plot reflected the conductivity of the material, charge transfer and carrier recombination kinetics during the photocatalytic process. As shown in Fig. 4b, the sample of UIO-66-NH₂/2.0GR exhibited a smaller capacitance arc than the pure UIO-66-NH₂, implying that the introduction of GR could enhance the electron mobility by reducing the recombination of photogenerated electron-hole pairs of UIO-66-NH₂. The Mott-Schottky plots (Fig. 4c) were also recorded based on the impedance measurements of UIO-66-NH₂ and UIO-66-NH₂/2.0GR, respectively. A positive Mott-Schottky plots slope was observed, suggesting that the as obtained samples were classified to the

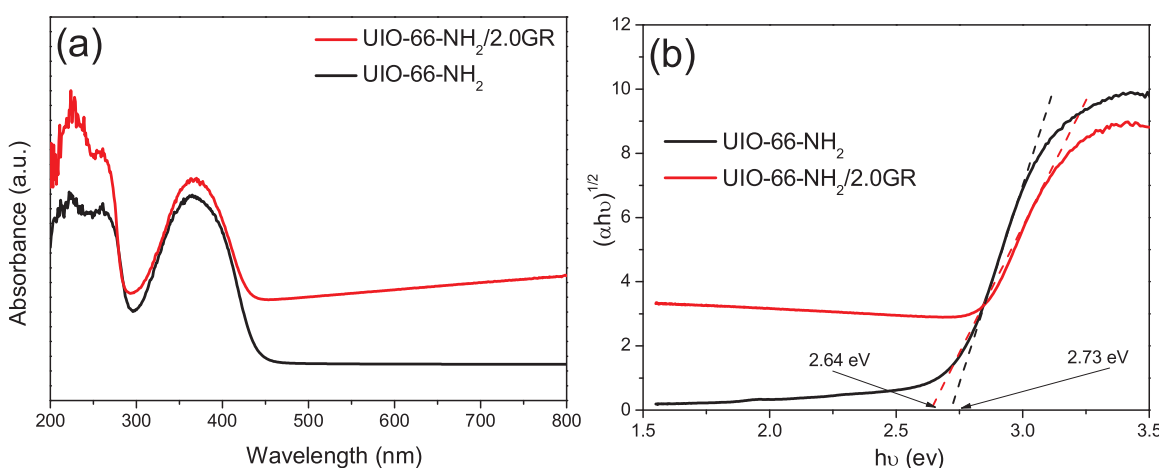


Fig. 3. The UV-vis absorption spectra of (a) and the determination of indirect inter-band transition energies (b) for both UIO-66-NH₂ and UIO-66-NH₂/2.0GR.

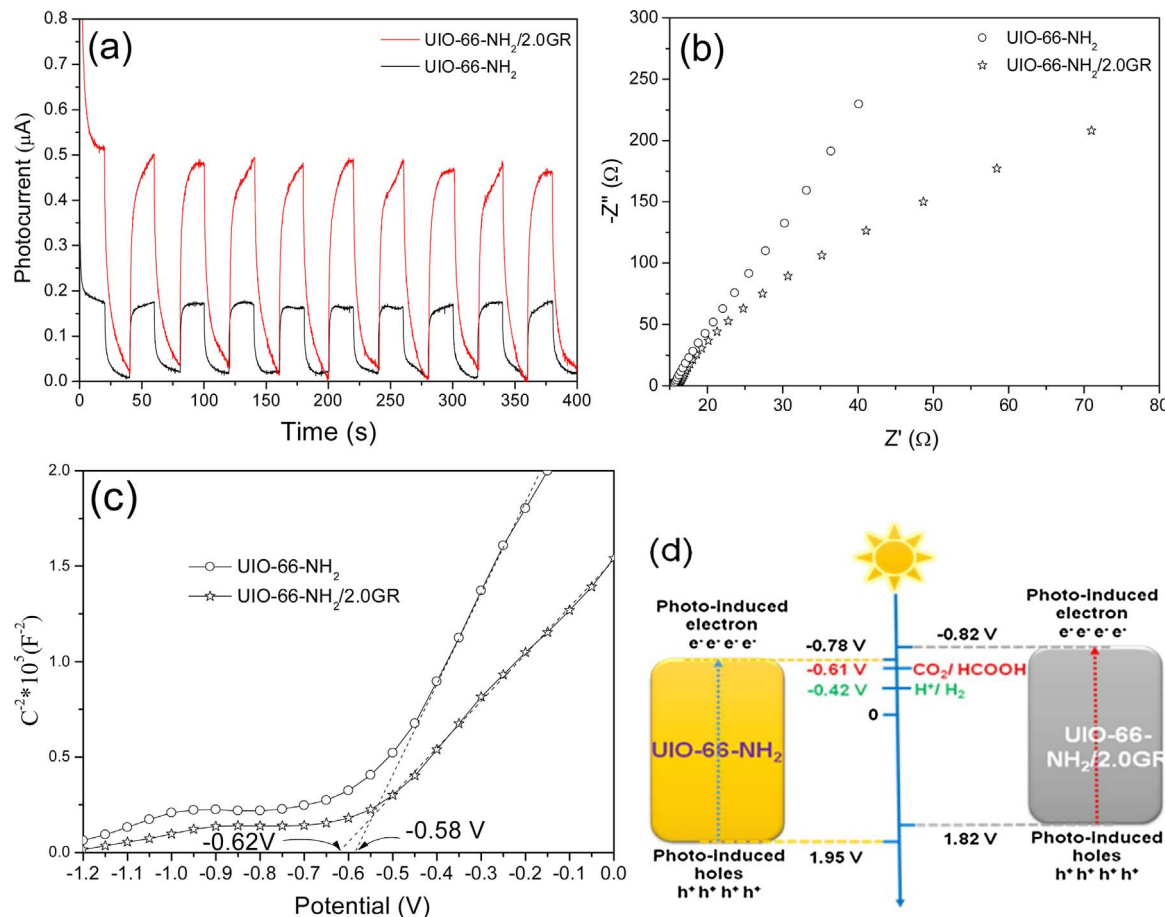


Fig. 4. Photocurrent spectra (a), electrochemical impedance spectroscopy (b), Mott-Schottky plots (c) according to impedance measurements, and potentials of valence and conduction bands (d) of GR and UIO-66-NH₂/2.0GR.

n-type semiconductor functional materials. The potential E_{fb} (Fermi level) of UIO-66-NH₂/2.0GR was about -0.62 eV , slightly negative than that of the pure UIO-66-NH₂ about -0.58 eV . Thus, the conduction bands (CB) of the two samples were -0.82 eV and -0.78 eV , respectively, because the CB of n-type semiconductors was more negative (about 0.2 eV) than the Fermi level. Taking account of the band gap resulted from UV-vis spectra, the band gap of both samples were 2.73 eV and 2.64 eV . Based on these results, the electronic energy band scheme was showed in Fig. 4d. The conduction band position of UIO-66-NH₂/2.0GR was enhanced from -0.78 eV to -0.82 eV , higher than the reduction potential of CO_2/HCOOH (-0.66 eV) [60,61]. A more negative conduction band position provided a stronger ability for photo-reducing CO_2 to HCOOH . Meanwhile, a low band gap (2.64 eV) was also favorable for improving the longer-wavelength light absorption [45]. Thus, these merits would allow the as-obtained photocatalysts to have stronger capability for reducing CO_2 to formic acid (Fig. 4d).

For evaluating the photocatalytic activity of the as-prepared samples, the reduction of CO_2 was performed under visible-light ($\lambda > 410 \text{ nm}$) irradiation in 50 mL DMF solution containing saturated CO_2 -Ar mixture gas (50 V%:50 V%). Fig. 5a and b showed the amount of CO_2 conversion and formic acid generation on the photocatalytic by using H_2O as the proton source and TEOA as sacrifice agent [56–62]. Besides, H_2 was also detected owing to the competitive reaction of hydrogen evolution. Low concentration of CH_4 was also detected as the product of CO_2 photo-reduction. In the presence of pure GR, nearly no photocatalytic activity was observed for the CO_2 reduction. All the samples of UIO-66-NH₂/GR exhibited much higher activity than the pure UIO-66-NH₂. As these results shown, the introducing of GR greatly

improved the photo-reduction performance of UIO-66-NH₂, owing to the increased conduction band of MOFs and decreased recombination rate of photogenerated electron-hole pairs. The introduction of GR effectively decreased the particle size of UIO-66-NH₂ from 23.5 nm to 14.0 nm and prevented the UIO-66-NH₂ particle from agglomeration effectively. Such ultrafine particles could also shorten the path of charge transfer from MOFs to GR, contributing an enhanced photo-reduction performance. It was observed that increasing the GR content may effectively enhance the photocatalytic activity for reducing CO_2 . The UIO-66-NH₂/2.0GR exhibited the highest HCOOH generation performance ($35.5 \mu\text{mol}$), about 11 times of that of the pure UIO-66-NH₂. However, over-loading GR ($> 2.0 \text{ wt\%}$) resulted in the decrease of the HCOOH production. Such decrease could result from the excessive GR, covering the active sites of the MOFs. It should be pointed out that both the conversion of CO_2 and the evolution of CH_4 exhibited similar trend as that of the evolution of HCOOH . These results also showed that the UIO-66-NH₂/2.0GR exhibited the highest selectivity (78.6%) of HCOOH for CO_2 photo-reduction (Table 1.). In addition, the introduction of GR could suppress the competitive reaction of hydrogen evolution as well. As shown in Fig. 5a, the sample of UIO-66-NH₂/2.0GR exhibited a lower hydrogen evolution amount ($13.2 \mu\text{mol}$) than that ($16.9 \mu\text{mol}$) of pure UIO-66-NH₂, while keeping high photocatalytic performance for reducing CO_2 to formic acid. To test the stability of the UIO-66-NH₂/2.0GR, a recycle measurement was performed. As shown in Fig. 5d, such high evolution of formic acid can be well maintained even after eight cycles of CO_2 photo-reduction under visible light irradiation. These results indicated that the MIS route was effective for the construction of excellent photocatalyst for reducing CO_2 at ambiences conditions with high activity and selectivity, as shown in Fig. 6.

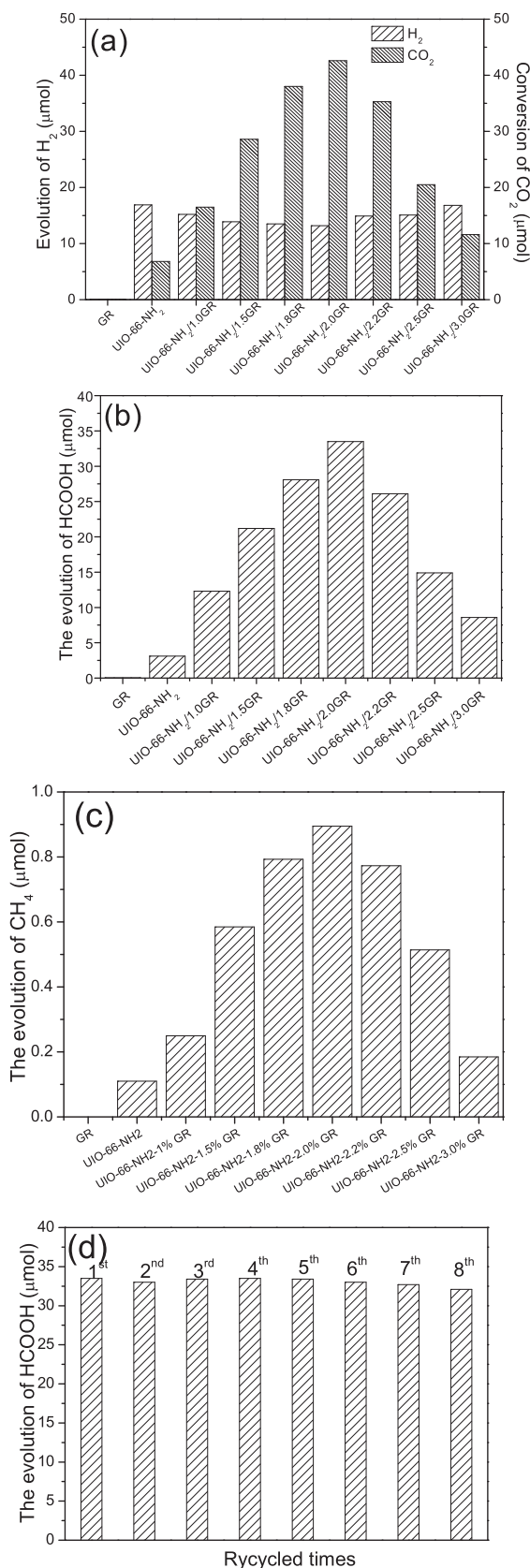


Fig. 5. The evolution of H_2 and the conversion of CO_2 (a), the evolution of formic acid (b) and CH_4 (c) of various photocatalysts under visible-light ($\lambda > 410$ nm) irradiation, and the recyclability of UIO-66-NH₂/2.0% GR for reducing CO_2 to formic acid (d).

To further demonstrate the advantages of the MIS route, various control experiments (obtaining the UIO-66-NH₂/2.0GR sample *via* hydrothermal method and mechanical mixing route) were carried out in the present work. The XRD patterns (Fig. S5) indicated that UIO-66-NH₂/2.0GR could be also synthesized *via* both the hydrothermal treatment and the mechanical mixing route. It was also noted that the microwave irradiation induced UIO-66-NH₂/2.0GR sample exhibited a great enhancement of visible-light absorption capability compared to other samples based on the UV-vis absorption spectra (Fig. S6). As the results showed, the sample synthesized by MIS route exhibited an excellent visible-light trapping ability. Therefore, the MIS induced UIO-66-NH₂/2.0GR sample reflected the highest photocurrent responses as shown in Fig. S7. The EIS measurements were also utilized to investigated the conductivity of the above three samples. The sample synthesized by the MIS route exhibited the smallest semicircle (Fig. S8), suggesting that the MIS induced sample possessed a tight junction between UIO-66-NH₂ and GR, resulting a better conductivity. As shown in Table 2, the MIS induced UIO-66-NH₂/2.0GR sample also exhibited the highest formic acid evolution amount for CO_2 photo-reduction (33.5 μmol), about 2.1 times of that (16.1 μmol) of the hydrothermal treatment induced sample, and 3.5 times of that (9.5 μmol) of the mechanical mixing sample. Such excellent photocatalytic performance could be attributed to the superiority of the MIS route. As known, the microwave irradiation route can produce local "super hot" dots on the surface of graphene [42]. Such local "super hot" dots were also beneficial for shaping the UIO-66-NH₂ crystals on the surface of graphene, resulting suitable particle size, high dispersity and tight junction between UIO-66-NH₂ and GR. These merits supplied a short pathway of charge transfer and low charge transfer resistance during the photocatalysis process [63]. Therefore, it was reasonable that the MIS route was proved as an effective strategy to synthesizing graphene hybrid photocatalytic materials.

4. Conclusions

The UIO-66-NH₂/GR composite functional material was synthesized via microwave-assisted *in situ* assembly of UIO-66-NH₂ onto GR. It exhibited excellent activity and selectivity in CO_2 photo-reduction under visible-light ($\lambda > 410$ nm) irradiation, much better than either the pure UIO-66-NH₂ or the UIO-66-NH₂/GR obtained via traditional hydrothermal synthesis. Such high photocatalytic activity for reducing CO_2 with high selectivity was mainly ascribed to the small particle size of MOFs crystals, high dispersion of UIO-66-NH₂ onto the surface of GR, strong CO_2 adsorption capability, and tight junctions between UIO-66-NH₂ and the surface of GR. Both small particle size and high dispersion may allow more light to be trapped for generating electron and holes pairs and supply a short electron transfer pathway for accelerating electron transfer from the bulk to the surface of MOFs crystals. Tight UIO-66-NH₂/GR junction may serve as electron transfer bridges for accelerating electrons transfer from MOFs to the UIO-66-NH₂/GR interaction surface, meanwhile, it can increase the stability of UIO-66-NH₂, avoiding leaching from GR. Such a microwave-assisted synthesis provided a promising method to fabricating highly efficient photocatalytic materials for CO_2 reduction.

Acknowledgements

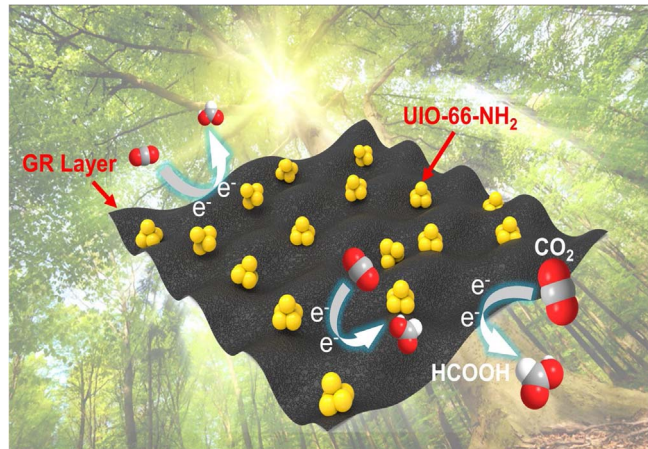
This work was supported by the National Natural Science Foundation of China (21207090, 21477079, 21677099), Shanghai Government Project (15QA1403300), and by a scheme administered by Shanghai Normal University (S30406).

Appendix A. Supplementary data

Supplementary material related to this article can be found, in the online version, at doi:<https://doi.org/10.1016/j.apcatb.2018.01.066>.

Table 1The conversion of CO₂, the evolution of various products, and the selectivity for formic acid of various catalysts.

Catalysts	CO ₂ reduction/μmol	H ₂ /μmol	CH ₄ /μmol	HCOOH/μmol	HCOOH selectivity/%
UIO-66-NH ₂	6.8	16.9	0.11	3.1	45.6
UIO-66-NH ₂ /1.0 GR	16.5	15.2	0.25	12.3	74.5
UIO-66-NH ₂ /1.5GR	28.6	13.9	0.59	21.2	74.1
UIO-66-NH ₂ /2.0GR	42.6	13.2	0.90	33.5	78.6
UIO-66-NH ₂ /2.5 GR	20.5	15.1	0.51	14.9	72.7
UIO-66-NH ₂ /3.0 GR	11.6	16.8	0.19	8.6	74.0

**Fig. 6.** The working mechanism of the UIO-66-NH₂/2.0% GR sample for reducing CO₂ to formic acid under visible light irradiation.**Table 2**The conversion of CO₂, the evolution of H₂ and formic acid, and the selectivity for formic acid of UIO-66-NH₂/2.0GR samples prepared with various synthesis routes.

Catalysts	UIO-66-NH ₂ /2.0GR	Conversion of CO ₂ /μmol	H ₂ /μmol	HCOOH/μmol	Selectivity for HCOOH%
Microwave	42.6	13.2	33.5	78.6	
Hydrothermal	23.9	20.4	16.1	67.4	
Mechanical	17.0	19.9	9.5	55.8	

Supplementary data associated with this article can be found in the online version. It includes some characterizations: TEM images, HRTEM, UV-vis absorbance, XRD, electrochemical impedance spectroscopy, Photocurrent spectra, and BET.

References

- [1] R. Marschall, *Adv. Funct. Mater.* 24 (2014) 2421–2440.
- [2] A. Kubacka, M. Fernández-García, G. Colón, *Chem. Rev.* 112 (2012) 1555–1614.
- [3] Z. Li, J. Feng, S. Yan, Z. Zou, *Nano Today* 10 (2015) 468–486.
- [4] S. Neātu, J.A. Maciá-Agulló, P. Concepción, H. García, *J. Am. Chem. Soc.* 136 (2014) 15969–15976.
- [5] S. Kumar, M.A. Isaacs, R. Trofimovaite, L. Durndell, C.M.A. Parlett, R.E. Douthwaite, B. Coulson, M.C.R. Cockett, K. Wilson, A.F. Lee, *Appl. Catal. B Environ.* 209 (2017) 394–404.
- [6] B. AlSabban, L. Falivene, S.M. Kozlov, A. Aguilar-Tapia, S. Ould-Chikh, J.L. Hazemann, L. Cavallo, J.M. Basset, K. Takanabe, *Appl. Catal. B Environ.* 213 (2017) 177–189.
- [7] Z.C. Lian, D.L. Pan, W.C. Wang, D.Q. Zhang, G.S. Li, H.X. Li, *J. Environ. Sci.* 60 (2017) 108–113.
- [8] Y. Lee, S. Kim, H. Fei, J.K. Kang, S.M. Cohen, *Chem. Commun.* 51 (2015) 16549–16552.
- [9] H.H. Wang, L. Hou, Y.Z. Li, C.Y. Jiang, Y.Y. Wang, Z. Zhu, *ACS Appl. Mater. Interfaces* 9 (2017) 17969–17976.
- [10] J.L. White, M.F. Baruch, J.E. Pander Iii, Y. Hu, I.C. Fortmeyer, J.E. Park, T. Zhang, K. Liao, J. Gu, Y. Yan, T.W. Shaw, E. Abelev, A.B. Bocarsly, *Chem. Rev.* 115 (2015) 12888–12935.
- [11] A. Genoni, D.N. Chirdon, M. Boniolo, A. Sartorel, S. Bernhard, M. Bonchio, *ACS Catal.* 7 (2017) 154–160.
- [12] C. Liu, K.D. Dubois, M.E. Louis, A.S. Vorushilov, G. Li, *ACS Catal.* 3 (2013) 655–662.
- [13] Z.C. Lian, W.C. Wang, S.N. Xiao, X. Li, Y.Y. Cui, D.Q. Zhang, G.S. Li, *Sci. Rep.* 5 (2015) 10461.
- [14] Q. Xu, J. Yu, J. Zhang, J. Zhang, G. Liu, *Chem. Commun.* 51 (2015) 7950–7953.
- [15] Z.C. Lian, W.C. Wang, G.S. Li, F.H. Tian, K.S. Schanze, H.X. Li, *ACS Appl. Mater. Interfaces* 9 (2017) 16960–16967.
- [16] A. Crake, *Mater. Sci. Technol.* (2017) 1–13.
- [17] L. Liu, H. Zhao, J.M. Andino, Y. Li, *ACS Catal.* 2 (2012) 1817–1828.
- [18] S.R. Lingampalli, M.M. Ayyub, C.N.R. Rao, *ACS Omega* 2 (2017) 2740–2748.
- [19] D. Wang, R. Huang, W. Liu, D. Sun, Z. Li, *ACS Catal.* 4 (2014) 4254–4260.
- [20] J. Ye, J.K. Johnson, *ACS Catal.* 5 (2015) 6219–6229.
- [21] M.C. Wen, K. Mori, Y. Kuwahara, H. Yamashita, *ChemCatChem* 7 (2015) 3519–3525.
- [22] M.C. Wen, K. Mori, Y. Kuwahara, T.C. An, H. Yamashita, *Appl. Catal. B Environ.* 218 (2017) 555–569.
- [23] D.L. Chen, S. Wu, P. Yang, S. He, L. Dou, F.F. Wang, *J. Phys. Chem. C* 21 (2017) 8857–8863.
- [24] Z. Hu, A. Nalaparaju, Y. Peng, J. Jiang, D. Zhao, *Inorg. Chem.* 55 (2016) 1134–1141.
- [25] G. Lv, J. Liu, Z. Xiong, Z. Zhang, Z. Guan, *J. Chem. Eng. Eng.* 61 (2016) 3868–3876.
- [26] P.C. Lemaire, D.T. Lee, J. Zhao, G.N. Parsons, *ACS Appl. Mater. Interfaces* 9 (2017) 22042–22054.
- [27] X. He, X. Min, X. Luo, *J. Chem. Eng.* 62 (2017) 1519–1529.
- [28] J.J. Zhou, R. Wang, X.L. Liu, F.M. Peng, C.H. Li, F. Teng, Y.P. Yuan, *Appl. Sur. Sci.* 346 (2015) 278–283.
- [29] J.L. Wang, C. Wang, W. Lin, *ACS Catal.* 2 (2012) 2630–2640.
- [30] J. Ye, J.K. Johnson, *ACS Catal.* 5 (2015) 2921–2928.
- [31] F. Yang, H. Huang, X. Wang, F. Li, Y. Gong, C. Zhong, J.R. Li, *Crys. Growth Des.* 15 (2015) 5827–5833.
- [32] H. Lv, H. Zhang, G. Ji, *Part. Part. Syst. Charact.* 33 (2016) 656–663.
- [33] L. Shen, W. Wu, R. Liang, R. Lin, L. Wu, *Nanoscale* 5 (2013) 9374–9382.
- [34] J. Low, J. Yu, W. Ho, *J. Phys. Chem. Lett.* 6 (2015) 4244–4251.
- [35] M. Xu, T. Liang, M. Shi, H. Chen, *Chem. Rev.* 113 (2013) 3766–3798.
- [36] A. Iwase, S. Yoshino, T. Takayama, Y.H. Ng, R. Amal, A. Kudo, *J. Am. Chem. Soc.* 138 (2016) 10260–10264.
- [37] Y. Zhou, Z. Mao, W. Wang, Z. Yang, X. Liu, *ACS Appl. Mater. Interfaces* 8 (2016) 28904–28916.
- [38] Y.T. Liang, B.K. Vijayan, K.A. Gray, M.C. Hersam, *Nano Lett.* 11 (2011) 2865–2870.
- [39] R. Kumar, D. Raut, U. Ramamurthy, C.N.R. Rao, *Angew. Chem. Int. Ed.* 55 (2016) 7857–7861.
- [40] T. Wang, C. Li, J. Ji, Y. Wei, P. Zhang, S. Wang, X. Fan, J. Gong, *ACS Sustain. Chem. Eng.* 2 (2014) 2253–2258.
- [41] R. Kumar, D. Raut, U. Ramamurthy, C.N. Rao, *Angew. Chem. Int. Ed.* 55 (2016) 7857–7861.
- [42] W. Zhu, P. Liu, S. Xiao, W. Wang, D. Zhang, H. Li, *Appl. Catal. B Environ.* 172 (2015) 46–51.
- [43] S. Xiao, P. Liu, W. Zhu, G. Li, D. Zhang, H. Li, *Nano Lett.* 15 (2015) 4853–4858.
- [44] S. Xiao, W. Zhu, P. Liu, F. Liu, W. Dai, D. Zhang, W. Chen, H. Li, *Nanoscale* 8 (2016) 2899–2907.
- [45] P. Daw, S. Chakraborty, G. Leitus, Y. Diskin-Posner, Y. Ben-David, D. Milstein, *ACS Catal.* 7 (2017) 2500–2504.
- [46] B. Cao, G. Li, H. Li, *Appl. Catal. B Environ.* 194 (2016) 42–49.
- [47] Z. Lian, P. Xu, W. Wang, D. Zhang, S. Xiao, X. Li, G. Li, *ACS Appl. Mater. Interfaces* 7 (2015) 4533–4540.
- [48] G. Li, B. Jiang, X. Li, Z. Lian, S. Xiao, J. Zhu, D. Zhang, H. Li, *ACS Appl. Mater. Interfaces* 5 (2013) 7190–7197.
- [49] X.H. Xia, Z.J. Jia, Y. Yu, Y. Liang, Z. Wang, L.L. Ma, *Carbon* 45 (2007) 717–721.
- [50] W. Hou, W.H. Hung, P. Pavaskar, A. Goepert, M. Aykol, S.B. Cronin, *ACS Catal.* 1 (2011) 929–936.
- [51] J. Shen, G. Liu, K. Huang, Q. Li, K. Guan, Y. Li, W. Jin, *J. Mem. Sci.* 513 (2016) 155–165.
- [52] F. Tuinstra, J.L. Koenig, *J. Chem. Phys.* 53 (1970) 1126–1130.
- [53] H. Jiang, P.S. Lee, C. Li, *Energy Environ. Sci.* 6 (2013) 41–53.
- [54] S. Xiao, D. Pan, L. Wang, Z. Zhang, Z. Lyu, W. Dong, X. Chen, D. Zhang, W. Chen, H. Li, *Nanoscale* 8 (2016) 19343–19351.
- [55] Z. Hu, Y. Peng, Z. Kang, Y. Qian, D. Zhao, *Inorg. Chem.* 54 (2015) 4862–4868.
- [56] D. Sun, Y. Fu, W. Liu, L. Ye, D. Wang, L. Yang, X. Fu, Z. Li, *Chem. Eur. J.* 19 (2013) 14279–14285.
- [57] Y. Kofuji, Y. Isobe, Y. Shiraishi, H. Sakamoto, S. Tanaka, S. Ichikawa, T. Hirai, *J. Am. Chem. Soc.* 138 (2016) 10019–10025.
- [58] H. Berndt, *J. Am. Chem. Soc.* 410 (1989) 81–91.
- [59] G. Li, Z. Lian, W. Wang, D. Zhang, H. Li, *Nano Energy* 19 (2016) 446–454.
- [60] C. Liu, T.R. Cundari, A.K. Wilson, *J. Phys. Chem. C* 116 (2012) 5681–5688.
- [61] W.H. Koppenol, J.D. Rush, *J. Phys. Chem.* 91 (1987) 4429–4430.
- [62] S. Zhu, S. Liang, Y. Tong, X. An, J. Long, X. Fu, X. Wang, *Phys. Chem. Chem. Phys.* 17 (2015) 9761–9770.
- [63] D. Zhang, P. Liu, S. Xiao, X. Qian, H. Zhang, M. Wen, Y. Kuwahara, K. Mori, H. Li, H. Yamashita, *Nanoscale* 8 (2016) 7749–7754.